PAPER

Check for updates

Enhancing long-term cycle stability of sodium-ion cathode materials *via* interlayer hydrogen bonding design

Minghui Zhong, [ab] Yi Li, [ab] Xingyu Li, [ab] Xiaolin Zhao*[ab] and Jianjun Liu 🆔 *[abc]

Polyanionic cathodes hold great potential for high-rate sodium-ion batteries (SIBs), yet structural instability caused by phase transitions remains a fundamental challenge for long-term cycling. Here, a new layered hybrid framework, $NaFePO_3CH_2PO_3H \cdot H_2O$ (NaFe-MDP), is designed by incorporating molecular-scale hydrogen bonding ($H-O-H \cdots O_3P-$) between coordinated water and organophosphonate groups. The bisphosphonate groups in the layered structure can be used as organic ligands to stabilize the transition metals and produce directional and saturated interlayer hydrogen bonds, which reinforces interlayer stability and suppresses detrimental phase transitions during cycling. Consequently, the NaFe-MDP electrode demonstrates exceptional long-term cycling stability, maintaining 87.7% of its initial capacity after 1000 cycles at a 4C rate. The hydrogen-bonding network's structural design, validated by DFT and crystal analysis, achieves one-dimensional Na^+ pathways with record ionic conductivity (up to $1.69 \times 10^{-9} \text{ cm}^2 \text{ s}^{-1}$). This work demonstrates a generalizable molecular design strategy for stabilizing layered polyanion cathodes in SIBs, offering novel perspectives on how stable hydrogen bonding regulates structural evolution and ion transport.

Introduction

Sodium-ion batteries (SIBs) are gaining traction as a long-life, environmentally resilient, and safe alternative to lithium-ion systems for grid-scale and high-power applications.[1,2] However, the success of high-performance cathode development hinges on materials that must demonstrate high ionic conductivity, excellent chemical and electrochemical stability, and ready availability of raw materials.[3] Unfortunately, traditional layered oxide cathodes, while offering substantial energy density, face challenges related to structural deterioration during cycling and inadequate thermal stability.[4] Moreover, the rigid structure of many polyanionic cathode materials can restrict ionic mobility, leading to suboptimal performance in high-rate applications.[5,6] Consequently, this presents a significant challenge in the development of suitable novel cathode materials with large migration channels to facilitate Na^+ ion movement while maintaining structural stability.

Conventional layered transition metal oxides are susceptible to phase transitions during charging due to sodium ion extraction and increased O–O repulsion.[7] Various modification strategies, such as metal/non-metal doping,[8,9] multiphase structural design,[10,11] structural nanosizing[12] and surface coating techniques,[13] are employed to the structural stability of cathode materials in SIBs. Among them, strengthening interlayer interactions has proven to be particularly effective.[14] Hydrogen bonding, a crucial intermolecular force in organic molecular stacking,[15,16] can also enhance interlayer interactions in inorganic materials, thereby improving structural stability and facilitating Na^+ ion migration. The organofunctional group phosphonic acid $-PO_3H_2$ not only forms hydrogen bonds but also coordinates with transition metals to create polyanion-like structures.[17] Medronic acid (MDP) with bisphosphonates is an important organophosphoric acid compound that can be used for drug delivery,[18] and as a surface modifier.[19] Additionally, it is effective in inhibiting scaling and corrosion.[20] More importantly, MDP usually serves as a stable coordination complex with multiple transition metal ions.

In this work, we demonstrate a layered cathode material NaFe-MDP with interlayer hydrogen bonding, which is expected to exhibit high cycling stability in SIBs. A robust structural framework was provided by bisphosphonate ligands, while the transition metal centers serve as electrochemically active sites for redox reactions during charge and discharge. Highly kinetic reactions of sodium ion diffusion were supported by both theoretical calculations and experimental results. During

[a]State Key Laboratory of High Performance Ceramics, Shanghai Institute of Ceramics, Chinese Academy of Sciences, 1295 Dingxi Road, Shanghai 200050, China. E-mail: jliu@mail.sic.ac.cn; zhaoxiaolin@mail.sic.ac.cn

[b]Center of Materials Science and Optoelectronics Engineering, University of Chinese Academy of Sciences, Beijing 100049, China

[c]School of Chemistry and Materials Science, Hangzhou Institute for Advanced Study, University of Chinese Academy of Science, 1 Sub-lane Xiangshan, Hangzhou, 310024, China

This journal is © The Royal Society of Chemistry 2025

J. Mater. Chem. A, 2025, **13**, 32375–32381 | **32375**

charging and discharging, the interlayer hydrogen bonding maintains the stability of the structure, potentially enabling NaFe-MDP to sustain high performance over 1000 cycles at a current density of 4C. Incorporating interlayer hydrogen bonding into layered structures could serve as a promising approach for designing next-generation sodium-ion battery cathode materials with extended cycle life.

Results and discussion

The XRD Rietveld refinement results (Fig. 1a) indicated that the single crystal phase NaFe-MDP belonged to the monoclinic structure with a space group of $C2/c$, exhibiting reliable R factors ($R_p = 10.1\%$, $R_{wp} = 13.6\%$). The refined Rietveld structure with the lattice parameters is presented in Fig. 1b, with atomic coordinates and occupation detailed in Table S1. From the b-axis direction, NaFe-MDP exhibited a layered structure stacked by interlayer hydrogen bonding, offering two distinct sites for sodium ion occupation. The intralayer $[NaO_6]$ octahedra were co-prismatic with $[FeO_6]$ along the b-axis, whereas the interlayer $[NaO_4]$ tetrahedra shared vertices with $[FeO_6]$ along the a-axis. Notably, water molecules within the NaFe-MDP structure

coordinated exclusively with iron ions. Additionally, the hydrogen atoms in coordinated water formed interlayer hydrogen bonds ($H-O-H\cdots O_3P-$) with oxygen atoms in $-PO_3$. Therefore, hydrogen bonding not only enhanced structural stability but also facilitated favorable channels for Na^+ migration.

The infrared spectra in the range of 400 to 4000 cm^{-1} (Fig. 1c) revealed a very strong absorption band between 1223 and 1278 cm^{-1}, attributed to strong hydrogen bonding involving the $H-O-H\cdots O_3P-$ groups.[21,22] The bands around 456 to 516 cm^{-1}, 1500 to 1680 cm^{-1} and 3237 to 3351 cm^{-1} correspond to the $\gamma(OH)$, $\delta(HOH)$ and $\nu(OH)$ of H_2O, respectively. The FTIR spectrum exhibited a broad band spanning from 938 cm^{-1} to 1165 cm^{-1}, attributed to phosphorus–oxygen (P–O) stretching vibrations. This was accompanied by well-defined peaks at 805 cm^{-1} and within the 2866–2998 cm^{-1} range, corresponding to $\delta(P-C-P)$ and $\nu(CH)$ groups, respectively.[21,23] The presence of water molecules was further confirmed by the solid-state ^1H MAS NMR spectrum (Fig. 1d), which showed two distinct peaks corresponding to the chemical shifts of H in H_2O (−1.739 ppm)[24] and $-CH_2$ (3.668 ppm),[25] respectively. Hydrogen bond
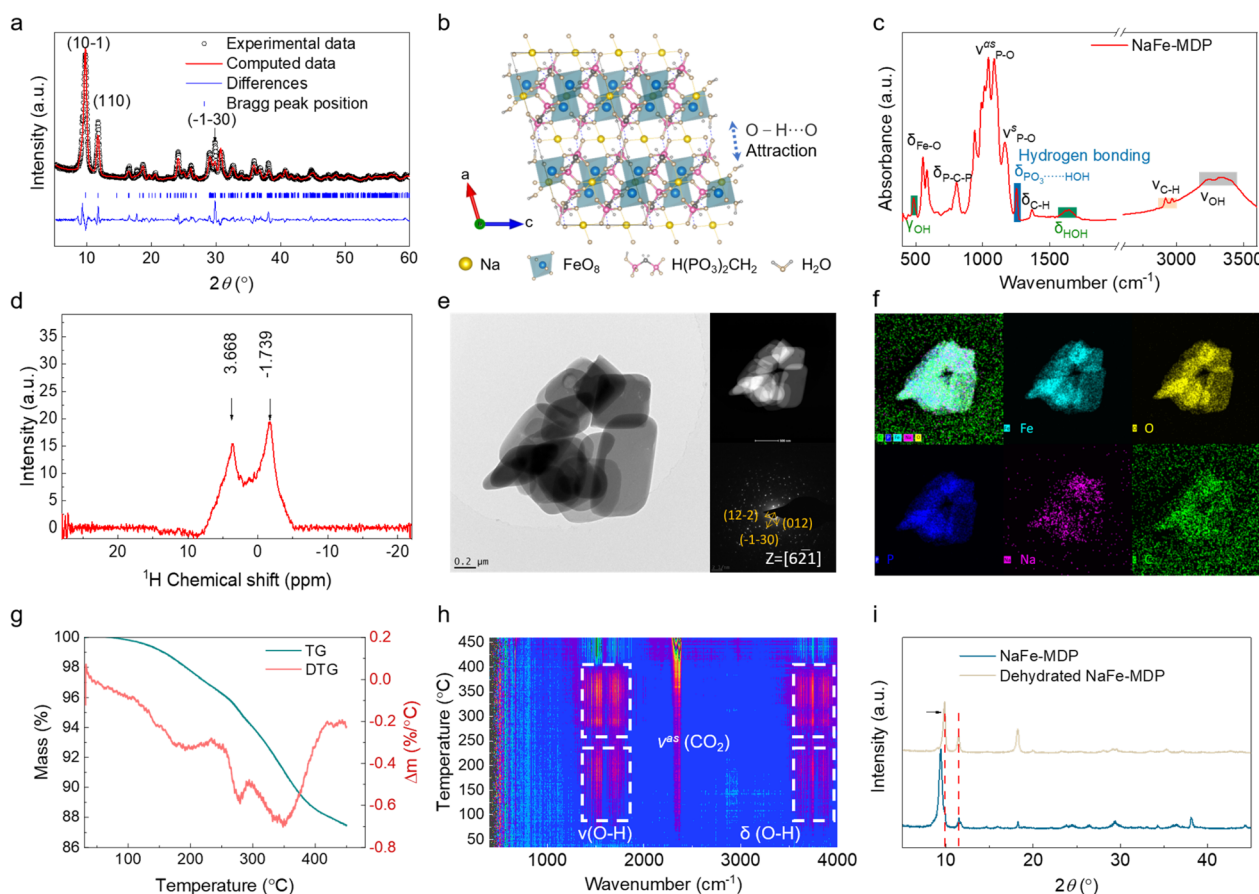

Fig. 1 (a) Comparison of calculated and experimental XRD patterns for NaFe-MDP. (b) Single crystal structure of NaFe-MDP; (c) the FIIR pattern of NaFe-MDP (δ: telescopic vibration, ν: bending vibration, γ: out-of-plane bending vibration, ν^s: symmetrical stretching vibration, ν^{as}: asymmetrical stretching vibration); (d) the ^1H MAS NMR spectra on a 600 MHz spectrometer; (e) TEM, HAADF and SEAD image of NaFe-MDP. (f) Elemental mapping of NaFe-MDP flakes; (g) thermogravimetric (TG) and derivative thermogravimetry (DTG) analysis of NaFe-MDP; (h) thermogravimetric analysis coupled with infrared spectroscopy (TG-IR) of NaFe-MDP; (i) XRD spectra comparison before and after vacuum-calcined at 180 °C.

32376 | *J. Mater. Chem. A*, 2025, **13**, 32375–32381

This journal is © The Royal Society of Chemistry 2025

formation leads to a decrease in the chemical bond's force constant, shifting the absorption frequency toward lower wavenumbers; simultaneously, the vibrational change in dipole moment enhances absorption intensity, often resulting in a broad and intense absorption peak.

The polycrystalline nature of NaFe-MDP was evidenced by High Angle Angular Dark Field-Scanning (HAADF) and the inset selected area electron diffraction (SAED) pattern (Fig. 1e), which corroborated the TEM images presented and aligned with prior XRD analysis findings. The average width of pure NaFe-MDP particles was determined to be approximately 1 μm exhibiting a two-dimensional lamellar structure (Fig. 1e). Elemental mapping of NaFe-MDP revealed that the elements C, Na, P, Fe, and O were uniformly distributed throughout the material (Fig. 1f). Thermogravimetric analysis coupled with infrared spectroscopy (TG-IR), as shown in Fig. 1g and h, revealed that crystalline water was desorbed at 180 °C. Without the hydrogen bonds provided by interlayer water molecules, the XRD patterns displayed a shift of diffraction peaks towards higher angles, as seen in Fig. 1i. This observation indicates a contraction of the interlayer spacing.

The electrochemical performance of NaFe-MDP was evaluated using a sodium metal anode cell within a voltage range of 1.5–4.2 V at a 0.1C rate (1C = 100 mA g^{-1}). The NaFe-MDP cathode exhibited an initial discharge capacity of 121.5 mA h g^{-1} at 1.5 V during its first discharge cycle (Fig. 2a). Compared to the initial charging capacity, the irreversible discharge specific capacity of 22.3 mA h g^{-1} was attributed to the production of the solid electrolyte phase.[26] The specific discharge capacity was 93.4, 90.4 and 85.6 mA h g^{-1} at the 2nd, 50th and 100th cycle, respectively, all with a coulombic efficiency of 100%. To characterize the electrode reactions in NaFe-

MDP, the dQ/dV curve was measured (Fig. 2b). The cyclic voltammetry (CV) plot of NaFe-MDP was scanned at 0.001 mV s^{-1} between 1.5 and 4.2 V (Fig. S1a). The pair of redox peaks at 2.24 V (oxidation) and 2.72 V (reduction) can be attributed to the Fe^{2+}/Fe^{3+} redox reaction.[27] Furthermore, no shift of the redox peak occurred during cycling, which confirmed the exceptional structural stability of NaFe-MDP. The rate performance of NaFe-MDP was evaluated under varying current densities (Fig. 2c). The specific capacity of NaFe-MDP decreased from 93.4 mA h g^{-1} to 63.0 mA h g^{-1} when the current was gradually increased from 0.1C to 2C. After 80 cycles with gradually increasing current densities, the specific discharge capacity returned to 93.4 mA h g^{-1} at 0.1C, demonstrating the excellent rate performance of the NaFe-MDP cathode.

Additionally, the structural stability of NaFe-MDP was further confirmed by its long cycle life at high rates, as shown in Fig. 2d. The cyclability of NaFe-MDP was demonstrated to be exceptional, maintaining 87.7% of its capacity after 1000 cycles at 4C and retaining 99% capacity after 700 cycles at 1C (Fig. S1b). As shown in the EIS of Fig. S1c, the interfacial impedance value for charge transfer increases and the Li-ion migration coefficient decreases after 1000 cycles, which may lead to a slight decrease in specific capacity after long-term cycling. Notably, the capacity of NaFe-MDP exhibited a slight increase within the first 100 cycles, which can be attributed to its activation process.[28] The Na$^+$ ion diffusion behavior in the layered NaFe-MDP cathode was examined through the application of the Galvanostatic Intermittent Titration Technique (GITT).[29] The calculated diffusion coefficient for Na$^+$ in the NaFe-MDP cathode ranged from 1.95×10^{-10} to 1.69×10^{-9} cm^2 s^{-1} (Fig. 2e). This commendable ionic conductivity was comparable to that of the inorganic layered materials S–
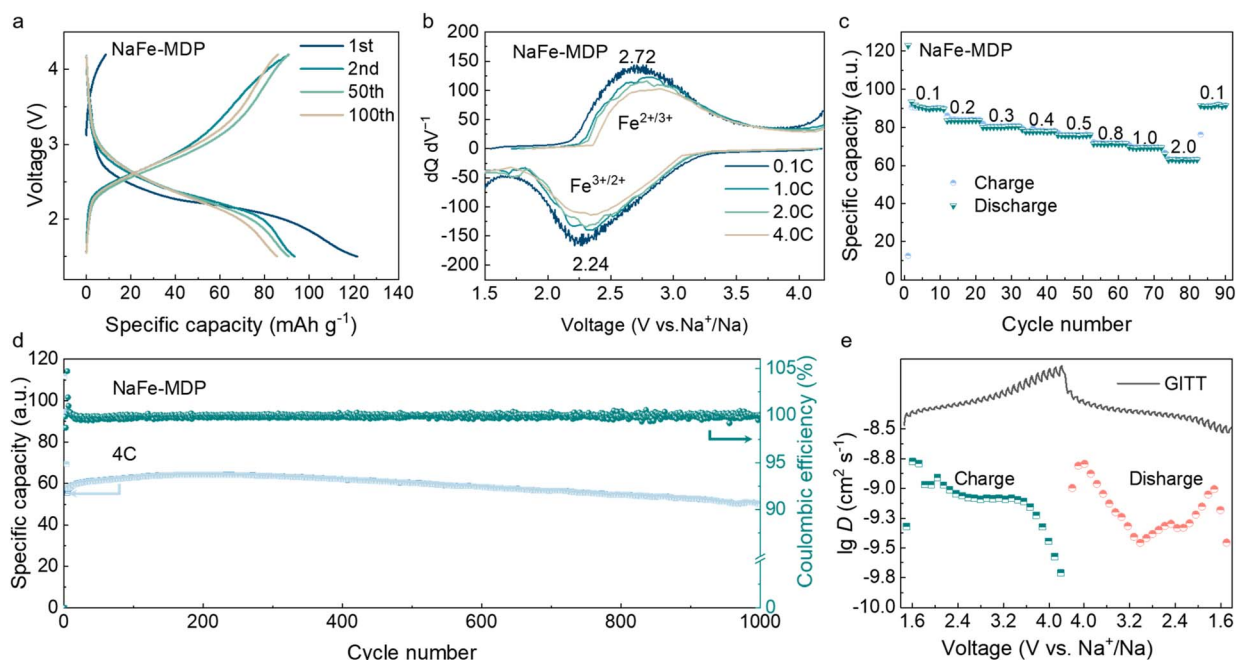

Fig. 2 (a) Galvanostatic charge/discharge (GCD) profiles at 0.1C within 1.5–4.2 V *vs.* Na$^+$/Na. (b) dQ/dV curves at various rates. (c) Rate performance. (d) The 1000th cycle of NaFe-MDP at 4C. (e) Logarithm of Na$^+$ diffusion coefficients (lg D) at discharge/charge states.

This journal is © The Royal Society of Chemistry 2025

J. Mater. Chem. A, 2025, **13**, 32375–32381 | **32377**

Na_xMnO_2 (5.1×10^{-11} cm^2 s^{-1}),[6] $Na_{0.61}Ca_{0.05}[Li_{0.1}Ni_{0.23}Mn_{0.67}]O_{1.95}F_{0.05}$ (1.249×10^{-11} cm^2 s^{-1})[30] and P2–$Na_{0.67}Ni_{0.33}Mn_{0.67}O_2$ (1.22×10^{-9} cm^2 s^{-1}).[31] A comparison of diffusion coefficients of Na^+ (D_{Na^+}) is shown in Table S2. This satisfactory ion migration rate is due to the presence of interlayer water molecules in NaFe-MDP. As shown in Fig. S2a, the ion mobility rate after dehydration of NaFe-MDP was significantly reduced. The slow sodium ion reaction kinetics resulted in dehydrated NaFe-MDP having a low specific capacity of 35 mA h g^{-1} (Fig. S2b). This result unequivocally demonstrates the critical role of interlayer water molecules in maintaining fast ion migration channels and enabling high-capacity electrochemical performance in NaFe-MDP.

The structural evolution of NaFe-MDP electrode materials during electrostatic charge/discharge cycling was examined using *in situ* XRD. The diffraction peaks located at 9.98° correspond to the crystal planes (10−1) (Fig. 3a). During charging to 4.2 V, the diffraction peak at 9.98° shifted to a lower Bragg angle (9.85°), indicating that the detachment of Na^+ caused lattice expansion. Upon discharging to 1.5 V, the position of the diffraction peak corresponding to the crystal plane (10−1) returned to its original position, confirming that the interlayer hydrogen bonding of bound water in NaFe-MDP facilitated reversible structural changes. The disappearance and reappearance of the (310) crystal plane were due to internal stress within the crystal. This stress caused the crystal planes to deviate from the Bragg condition, temporarily eliminating the diffraction peak. When the stress was relieved or redistributed,

the crystal planes realign, restoring the (310) diffraction peak. Notably, the continuous emergence of peaks in the 35–40° Bragg range during this period highlighted the crystal's excellent structural stability. The diffraction peaks at 26.78° and 43.70° were attributed to conducting carbon, as observed in the *ex situ* XRD spectrum (Fig. S3). Moreover, the structural stability under long-range cycling was further characterized. After 1200 cycles, the NaFe-MDP cathode retained its characteristic diffraction peaks at 9.7° and 11.6° (Fig. S4), confirming the preservation of the primary framework. However, the appearance of a broad hump around 20° indicated partial loss of crystallinity, suggesting the formation of localized disordered domains while maintaining overall structural integrity. Transmission electron microscopy (TEM) analysis before and after cycling (Fig. S5) revealed that the material exhibited a uniform distribution of elements but with diminished crystallinity. This observation was leveraged to elucidate the gradual capacity decay following prolonged cycling.

Absorption bands corresponding to water molecule vibrations were observed in the FTIR spectra of the redox reactions during charge and discharge (Fig. 3b). The telescopic vibration band, $\delta(HOH)$, was observed in the range of 1500–1550 cm^{-1}. The frequency of the $\delta(HOH)$ bending modes indicated the strong coordination of water molecules and the presence of hydrogen bonding within the structure.[32,33] The $\delta(P–C–P)$ and $\nu(CH)$ bending modes remained unchanged during charging and discharging, indicating ligand stability following electrochemical cycling. Similarly, the Raman spectra in Fig. S6
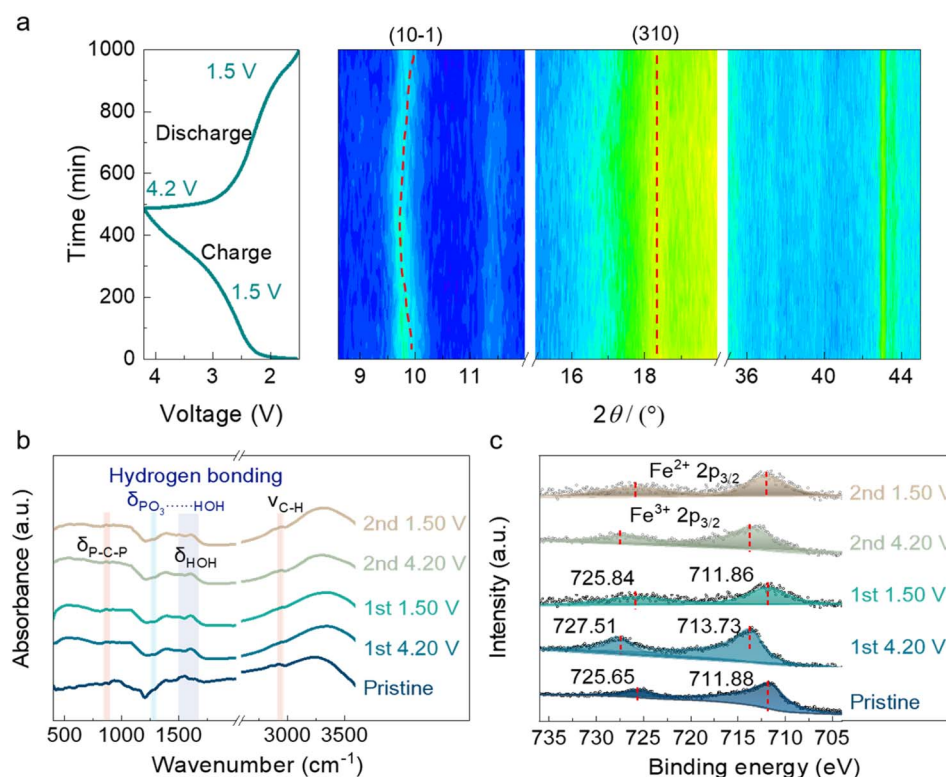

Fig. 3 (a) *In situ* XRD patterns of NaFe-MDP during the second charge/discharge cycle. (b) FTIR spectra of H-bonds in the cathode after discharge/charge. (c) Binding energy of Fe 3d during a full charge/discharge cycle.
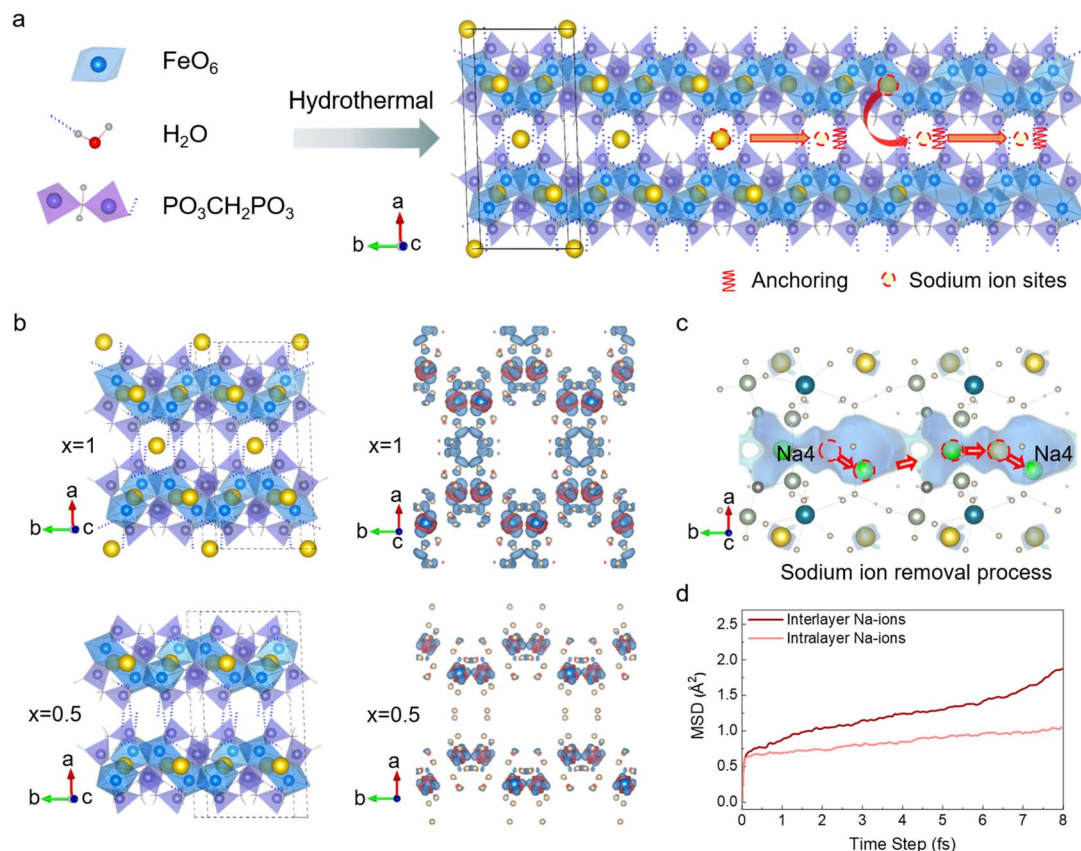
32378 | *J. Mater. Chem. A*, 2025, **13**, 32375–32381

This journal is © The Royal Society of Chemistry 2025

Fig. 4 (a) NaFe-MDP synthesis pathway and Na⁺ removal process of Na$_x$Fe-MDP along the b-direction; (b) the crystal structure and charge density maps of Na$_1$Fe-MDP and Na$_{0.5}$Fe-MDP with cyan/pink = ±0.006 Å^{-3}; (c) optimal 1D Na⁺ migration path overlaid on the crystal structure (light purple isosurface of $E_{BVSE(Na)}$); (d) MSD plots of C, O, H, P, Fe, and Na atoms at 553 K.

revealed a persistent broad peak spanning the 2300–3400 cm^{-1} range,[34] indicative of hydrogen bonding throughout the charging and discharging processes.

The XPS results of Fe 2p in Fig. 3c were used to examine the redox reactive sites of NaFe-MDP during charging and discharging. Prior to electrochemical cycling, analysis revealed that the iron (Fe) in the pristine NaFe-MDP cathode was predominantly present as Fe^{2+}, as evidenced by the Fe2p$_{3/2}$ peak at 711.88 eV and the 2p$_{1/2}$ peak at 725.65 eV characteristic of Fe^{2+}.[27] Upon charging completion, dominant Fe^{3+} peaks appeared at 713.73 eV and 727.51 eV, demonstrating an oxidation state transition of Fe from +2 to +3. Upon discharging to 1.5 V, these peaks shifted to lower binding energies (711.86 eV and 725.84 eV), reverting to Fe^{2+} species once again. The same change in peak position occurred during the second cycle, suggesting that iron acted as a reversible redox site in the electrochemical process.

The sodium storage mechanism of NaFe-MDP featuring interlayer hydrogen bonding was investigated through first-principles calculations, focusing on structural evolution, sodium ion migration dynamics, and charge distribution during charge/discharge cycles. The calculated lattice parameters (Table S3) of NaFe-MDP closely matched the experimental data (Table S1), demonstrating calculation accuracy. In contrast to traditional inorganic layered materials, the hydrogen bonds

formed between H–O–H and O_3P– within the interlayers of NaFe-MDP are essential for preserving structural integrity. During charging, sodium ions were first preferentially released from the interlayer region (Fig. 4a) and subsequently deintercalated from the transition metal layer.

Additionally, the lattice parameter b (Table S3) demonstrated an increasing trend during sodium ion removal, which aligns with the observed decrease in the Bragg angle for the (10−1) crystal plane as captured in the *in situ* XRD measurements. The charge voltages of Na$_x$Fe-MDP were calculated based on the Gibbs energy of Na$_x$Fe-MDP Na⁺ occupancy sites for $x = 1$, 0.5 and 0 (Fig. S7a). The calculated charging voltage for sodium ion detachment was 2.77 V (Fig. S7b), which closely matches the experimental charging potential (2.72 V). However, the potential for sodium ion de-intercalation within the transition metal layer was higher than the experimental value, which may be attributed to the slow reaction kinetics of sodium ions within the transition metal layer. In order to confirm that the iron displacement reaction does not occur within the voltage window of 4.2–1.5 V, based on the Gibbs free energy of the structure before and after the precipitation of iron (Fig. S7c), we calculated the redox potential of NaFe^{II}-MDP + 0.25Na⁺ → 0.125Fe^0 + Na$_{1.25}$Fe$_{0.875}^{II}$-MDP, which is 1.14 V (Fig. S7d), significantly lower than the discharge cutoff potential of 1.5 V. This indicated that the sodium ion de/

This journal is © The Royal Society of Chemistry 2025

J. Mater. Chem. A, 2025, **13**, 32375–32381 | **32379**

intercalation is based on the redox of Fe^{2+}/Fe^{3+} at experimental voltages of 4.2–1.5 V.

The charge transfer mechanism was explained by differential charge analysis of the atomic-scale charge redistribution pathways during charging. The structures of Na_xFe-MDP were determined by optimizing the lowest energy Na^+ occupancy sites for $x = 0.5$ and 0 (Fig. 4b). The pink area of charge density difference mapping indicated interfacial charge accumulation, while the cyan area signified charge depletion. The electron cloud around Fe ions had reduced and O atoms maintained a constant charge during charging, demonstrating that the redox site was iron as corroborated by XPS, CV and dQ/dV. The projected density of states (pDOS) analysis of Na_xFe-MDP revealed that Fe 3d orbitals donate electrons for electrochemical processes during Na-ion extraction (Fig. S8).

Molecular dynamics (MD) simulations explain the kinetic behavior and structural stability of NaFe-MDP. Sodium ions transition states migrate along the [010] channel of NaFe-MDP (Fig. 4c), where the highest migration energy barrier of 0.837 eV was calculated using the BVSE method (Fig. S9a). MD simulations were performed at 553 K and then a diffusion coefficient value of 9.83×10^{-8} cm^2 s^{-1} was obtained by mean squared displacement (MSD), which closely aligns with the experimentally determined value (1.69×10^{-9} cm^2 s^{-1}) (Fig. 4d). Moreover, the average H-bond length of 0.97 Å in water molecules (Fig. S9b) indicated stable NaFe-MDP during Na^+ diffusion. In addition, molecular dynamics simulations show that removing water molecules causes the collapse of the Fe–oxygen octahedra (Fig. S9c), with Fe migration blocking the Na ion pathway. Comparing the iron migration paths before and after dehydration of NaFe-MDP (Fig. S9d and e) revealed that in hydrated NaFe-MDP, iron stayed at its equilibrium position. This observation was corroborated by EIS data from Fig. S2a, obtained prior to battery cycling. By performing DFT calculations on NaTM-MDP materials (TM: Ti, V, Cr, Mn, Fe, Co, Ni, Cu), it can be seen in Fig. S10 that NaMn-MDP and NaCo-MDP exhibit similar specific capacities, charging voltages, and sodium-ion migration barriers to NaFe-MDP, which are expected to be used as cathode materials for sodium-ion batteries.

Conclusions

In this study, a layered polyanionic nanocomposite was fabricated via a straightforward hydrothermal synthesis. The structural stability during sodium ion extraction was maintained through hydrogen-bonding interactions arising from interlayer water molecules, which counteracted lattice distortions induced by ion deintercalation. Electrochemical evaluations revealed that NaFe-MDP demonstrated exceptional electrochemical resilience, preserving over 80% of its initial capacity following 1000 cycles at a current density of 4C. Specifically, the capacity retention remained at 87.7% after these extensive cycling conditions. This study presents a promising, sustainable strategy for achieving structural stability, potentially guiding advancements in other polyanionic cathode materials and beyond.

Author contributions

M. Zhong: methodology, investigation, data curation, visualization, formal analysis, writing – original draft. Y. Li and X. Li: validation. J. Liu and X. Zhao: conceptualization, funding acquisition project administration, resources, software, conceptualization, methodology, writing – review and editing.

Conflicts of interest

There are no conflicts to declare.

Data availability

The data that support the findings of this study are available from the corresponding author upon reasonable request.

Supplementary information is available. Chemistry and materials, characterization, electrochemical measurements, and calculations used in this study. See DOI: https://doi.org/10.1039/d5ta04305k.

Acknowledgements

References

1 J. Zhang, Y. Yan, X. Wang, Y. Cui, Z. Zhang, S. Wang, *et al.*, *Nat. Commun.*, 2023, **14**, 3701.

2 V. Shipitsyn, R. Jayakumar, W. Zuo, B. Sun and L. Ma, *Batteries*, 2023, **9**, 461.

3 Z. Liang, F. Tian, G. Yang and C. Wang, *Nat. Commun.*, 2023, **14**, 3591.

4 Q. Wang, D. Zhou, C. Zhao, J. Wang, H. Guo, L. Wang, *et al.*, *Nat. Sustain.*, 2024, 7, 338.

5 X. Li, Y. Meng and D. Xiao, *Chem.–Eur. J.*, 2023, **29**, 338.

6 J. Nanda, *Nat. Energy*, 2024, **9**, 1457.

7 W. Zuo, X. Liu, J. Qiu, D. Zhang, Z. Xiao, J. Xie, *et al.*, *Nat. Commun.*, 2021, **12**, 4903.

8 H. Zhang, Y. Cao, Z. Liu, X. Cheng, X.-L. Li, J. Xu, *et al.*, *ACS Sustainable Chem. Eng.*, 2024, **12**, 5310.

9 S. D. Shraer, N. D. Luchinin, I. A. Trussov, D. A. Aksyonov, A. V. Morozov, S. V. Ryazantsev, *et al.*, *Nat. Commun.*, 2022, **13**, 4097.

10 Y.-F. Liu, H.-Y. Hu, Y.-F. Zhu, D.-N. Peng, J.-Y. Li, Y.-J. Li, *et al.*, *Chem. Commun.*, 2024, **60**, 6496.

11 X. Xu, S. Ren, H. Wu, H. Li, C. Ye, K. Davey, *et al.*, *J. Am. Chem. Soc.*, 2024, **146**, 1619.

12 M. Choi, H. Shin, D. Kim and W. Choi, *J. Am. Chem. Soc.*, 2024, **615**, 235066.

32380 | *J. Mater. Chem. A*, 2025, **13**, 32375–32381

This journal is © The Royal Society of Chemistry 2025

13 G. Minart, L. Croguennec, F. Weill, C. Labrugère-Sarroste and J. Olchowka, *ACS Appl. Energy Mater.*, 2024, **7**, 11253.

14 L. Feng, Y. Gong and J. Lin, *Chem. Eng. J.*, 2024, **493**, 152612.

15 T. Li, Y. Xiao, X. Hao, Y. Li and W. Wang, *Carbon*, 2024, **228**, 119309.

16 V. Durán-Egido, J. P. Darby, M. J. Cliffe, J. S. Garitaonandia, P. Grande-Fernández, A. J. Morris, *et al.*, *Angew. Chem., Int. Ed.*, 2025, **64**, e202424416.

17 G. Yucesan, V. Golub, C. J. O'Connor and J. Zubieta, *Inorg. Chim. Acta*, 2006, **359**, 1637.

18 Y.-T. Lin, S.-A. Chan, Y.-J. Chen, K.-P. Chung and C.-H. Kuo, *J. Proteome Res.*, 2023, **22**, 1434.

19 J. S. Barbosa, F. A. Almeida Paz and S. S. Braga, *J. Med. Chem.*, 2021, **64**, 1260.

20 J. J. Hsiao, O. G. Potter, T.-W. Chu and H. Yin, *Anal. Chem.*, 2018, **90**, 9457.

21 K. Moedritzer and R. R. Irani, *J. Inorg. Nucl. Chem.*, 1961, **22**, 297.

22 K. Xu, R. Oestreich, T. Haj Hassani Sohi, M. Lounasvuori, J. G. A. Ruthes, Y. Zorlu, *et al.*, *Nat. Commun.*, 2024, **15**, 7862.

23 D. De Alwis Jayasinghe, Y. Chen, J. Li, J. M. Rogacka, M. Kippax-Jones, W. Lu, *et al.*, *J. Am. Chem. Soc.*, 2024, **146**, 32040.

24 L. Al Fuhaid, M. F. Nava-Ocampo, S. S. Bucs, R. Verpoorte, Y. H. Choi, G.-J. Witkamp, *et al.*, *J. Mol. Liq.*, 2023, **387**, 122718.

25 E. Brunner and U. Sternberg, *Prog. Nucl. Magn. Reson. Spectrosc.*, 1998, **32**, 21.

26 Y. B. Niu, Y. J. Guo, Y. X. Yin, S. Y. Zhang, T. Wang, P. Wang, *et al.*, *Adv. Mater.*, 2020, **32**, 2001419.

27 J. Geng, Y. Ni, Z. Zhu, Q. Wu, S. Gao, W. Hua, *et al.*, *J. Am. Chem. Soc.*, 2023, **145**, 1564.

28 J. Hu, W. Tang, Y. Hong, B. Wei, S. Jia, M. Guo, *et al.*, *J. Energy Storage*, 2023, **73**, 108901.

29 G. Li, Y. Cao, J. Chen, K. Zhang, Y. Liu, X. Zhang, *et al.*, *Small Methods*, 2024, **8**, 2301745.

30 X. Liu, C. Yuan, X. Zheng, G. Cheng, H. Qian, B. Zheng, *et al.*, *Adv. Mater.*, 2024, **36**, 2407519.

31 M. Gao, H. Li, Z. Zhao and X. Wang, *ACS Appl. Mater. Interfaces*, 2024, **16**, 14789.

32 P. Piszczek, A. Grodzicki and B. Engelen, *J. Mol. Struct.*, 2003, **646**, 45.

33 C.-C. Yu, K.-Y. Chiang, M. Okuno, T. Seki, T. Ohto, X. Yu, *et al.*, *Nat. Commun.*, 2020, **11**, 5977.

34 Z. Khan, D. Kumar and X. Crispin, *Adv. Mater.*, 2023, **35**, 2300369.

This journal is © The Royal Society of Chemistry 2025

J. Mater. Chem. A, 2025, **13**, 32375–32381 | **32381**